This article has been accepted for publication in IEEE Sensors Journal. This is the author's version which has not been fully edited and content may change prior to final publication. Citation information: DOI 10.1109/JSEN.2024.3409535

Titanium Dioxide-Graphene-Black Phosphorus-Based SPR Sensor for Helicobacter Pylori Bacteria Detection

Yesudasu Vasimalla, Shivam Singh, *Member*, *IEEE*, Ganta Raghotham Reddy, Rajeev Kumar, *Member*, *IEEE*, Suman Maloji, Santosh Kumar, *Senior Member, IEEE*

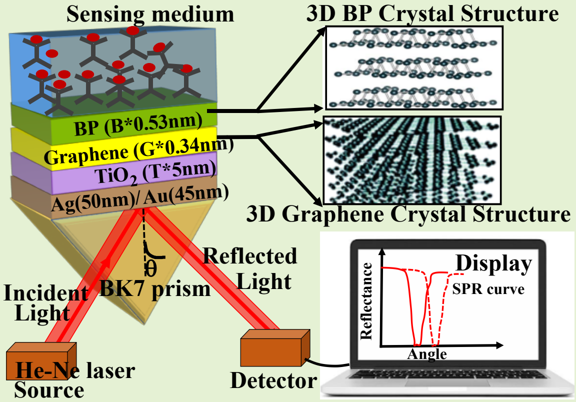

***Abstract*— Helicobacter pylori (*H. pylori*) plays a significant role in the development of various gastrointestinal diseases. It is a form of bacteria that infects the first part of the small intestine (duodenum). This bacterium is a common cause of peptic ulcers. This paper presents two surface plasmon resonance (SPR) sensors for the detection of *H. pylori*. Sensors 1 and 2 consist of a structure of prism-Ag-TiO_2-graphene-BP-SM and prism-Au-TiO_2-graphene-BP-SM, respectively. This work takes advantage of the excitement of surface plasmons and evanescent waves at the metal-dielectric interface. The angular interrogation technique is used to analyze the proposed sensors at a wavelength of 633 nm. Results show that sensor 1 furnishes the maximum sensitivity of $321.43^{\circ}/RIU$, Quality factor (QF) of 57.09RIU^{-1}, dip of figure of merit (DFoM) of 5974.53 and Combined sensitive factor (CSF) of 52.63, and sensor 2 endows the maximum sensitivity of $261.25^{\circ}/RIU$, QF of 30.41RIU^{-1}, DFoM of 22, 139 and CSF of 28.21. The results furnish a substantial improvement in comparison to the reported work in the literature. Finally, the field distributions of the proposed sensor are exhibited using the COMSOL software.**

***Index Terms*— Black phosphorus, graphene, Helicobacter pylori, Optical biosensors, surface plasmon resonance**

I. INTRODUCTION

HELICOBACTER pylori (*H. pylori*) is a type of bacteria that infects the stomach or the first part of the small intestine (duodenum). This bacterium is a common cause of peptic ulcers, and it's known to play a significant role in the development of various gastrointestinal diseases. Nevertheless, Marshall and Warren made the discovery of *H. pylori*'s existence thirty years ago [1]. It is still uncertain which standard may be used for *H. pylori* detection in epidemiological investigations. Generally**,** an endoscopy plus a blood test can be used to identify *H. pylori*. The blood test's result could include some false negatives because it's a simpler test [2]. Although the endoscopic examination is more accurate, time consumption becomes a crucial element when dealing with a large number of patients. Additionally, direct techniques like immunohistochemistry (IHC), the rapid urease test (RUT), and culture can be used to diagnose *H. pylori*. In essence, information about genotype and antibiotic resistance is provided by these direct approaches. However, the sensitivity performance of such direct diagnosis schemes is reduced when there are only a few bacteria present in the stomach. As a result, various indirect methods, including stool antigen testing (SAT), urine breath testing (UBT), and urine assays, were found to be effective in diagnosing the presence of *H-pylori* [3]. With a sensitivity of 99%, UBT was thought to be the most accurate method among all of them [4]. Even so, a meta-analysis found that the SAT aims for more than 90% in terms of both sensitivity and specificity [5]. Similar to this, *H. pylori* can be identified using affordable, non-biomolecule-affecting serological testing (based on antibodies). But, compared to UBT and SAT, these serological tests are less accurate,

---

(Corresponding authors: Yesudasu Vasimalla and Santosh Kumar)

Yesudasu Vasimalla, Suman Maloji and Santosh Kumar are with the Department of Electronics and Communication Engineering, Koneru Lakshmaiah Education Foundation, Vaddeswaram, Andhra Pradesh 522302, India (e-mail: vasimalladasu@gmail.com, suman.maloji@kluniversity.in and santosh@kluniversity.in).

Shivam Singh is with Department of Electronics and Communication Engineering, ABES Engineering College, Ghaziabad 201009, Uttar Pradesh, India (e-mail: shivams20@gmail.com)

Ganta Raghotham Reddy is with the department of Electronics and Communication Engineering at Kakatiya Institute of Technology and Sciences, Warangal, Telangana – 506015, India (grrece9@gmail.com)

Rajeev Kumar is with Department of Electronics and Communication Engineering, Graphic Era Deemed to be University, Dehradun 248002, Uttarakhand, India (e-mail: rajeevkrc@gmail.com)

particularly in regions where the frequency of *H. pylori* is low [6]. On the other hand, in high-prevalence locations, if there are no other options, a positive serology test may be taken into consideration [7]. Even after considering the aforementioned methods and their drawbacks, an ideal sensor model is still required for the more sensitive and accurate diagnosis of *H. pylori*. Consequently, in this work, we propose an optical sensor, which is refractive index (RI)-based, for diagnosing the *H. pylori*. Optical sensors offer greater sensitivity and immunity to electromagnetic interference (EMI) when compared to other transduction methods. [8]. For the purpose of measuring RI, an optical sensor based on the Kretschmann-Raether arrangement is suggested [9]. A plasmonic switch functionalized with graphene and based on the Goos-Hanchen phenomenon is presented. The switch may be used to monitor the impacts of temperature, scattering time, and chemical potential because of its bidirectional wide tuning design [10]. The exhibited sensor uses the provision of surface plasmon waves (SPWs), which are produced when surface plasmon resonance (SPR) happens at the metal-dielectric interface. Due to its label-free and real time application, SPR is highly popular in different applications, such as sensing chemical, physical, and biological factors [11], [12]. Particle oscillations at the metal-dielectric interface are excited in SPR by transverse magnetic (TM) polarized light [13]. The SPR-generated field decays exponentially in both metallic and dielectric layers, with the greatest effect occurring at the metal-dielectric boundary. Nonetheless, in a traditional prism-based arrangement, light incident at an angle greater than the critical angle follows the principle of total internal reflection in the prism base [14]. At the metal-dielectric interface, SPR production should satisfy the resonance condition of Eq. (1), where k_0, n_p, θ_{res}, ϵ_m and n_d represent propagation constant of free-space, prism's RI, resonance angle of a SPR curve and RI of dielectric layer that is in contact with the metallic layer. The left side part of Eq. (1) demonstrates the evanescent wave, whereas right side part represents the SPW's propagation constant [15].

$$k_0 n_p \sin\theta_{res} = k_0\sqrt{\frac{\epsilon_m n_d^2}{\epsilon_m + n_d^2}} \tag{1}$$

The most widely utilized metal films for the formation of surface plasmon polaritons (SPPs) are silver (Ag) and gold (Au), according to the literature on SPR sensors [16], [17]. Ag was selected as a plasmonic layer in our investigation because of its high SPR ratio, which is defined as the ratio of the dielectric constant's real and imaginary components' absolute values [18]. In addition to conferring increased sensitivity, the SPR ratio defines the proportion of the real and imaginary sections of the dielectric constant, expressed in absolute numbers [1]. Similarly, Au's electronic properties make SPR sensors extremely sensitive to changes in the RI near the sensor surface. This allows for the detection of very small amounts of a substance, making it an invaluable tool for analyzing low concentrations of analytes. Moreover, its unique optical properties, like chemical stability, biocompatibility, sensitivity, versatility, and durability—make it the metal of choice for these devices, facilitating the detailed study of molecular interactions with high sensitivity and specificity [19]. Label-free sensing with greater sensitivity is offered by SPR biosensors. Rather than offering significant benefits, SPR biosensors are unsuitable for measuring biomolecule concentrations below 200 daltons. To address the drawbacks of SPR sensors, various strategies have been employed [1], [19]–[21]. A ten-fold increase in sensitivity over conventional SPR sensors is possible with nanoparticle-based sensors [20]. Nevertheless, the immobilization of nanoparticle layers results in a decrease in reflectivity dip penetration, which limits the sensor's ability to detect [22].

With this concern, this paper utilizes titanium dioxide ($\mathrm{TiO_2}$) composed over the metallic layer to protect the metallic layer and enhance the sensing capability due to high RI value. Moreover, $\mathrm{TiO_2}$ coatings can minimize background noise in SPR measurements by reducing nonspecific adsorption of biomolecules onto the sensor surface. Also, it provides a stable and biocompatible surface for immobilizing biomolecules such as antibodies or deoxyribonucleic acid (DNA) probes, which are used for specific binding interactions in biosensing applications. TiO_2 has a wide bandgap energy, typically around 3.0 to 3.2 eV for the anatase phase and 3.2 to 3.4 eV for the rutile phase [21], [23].

Besides, graphene, with its remarkable properties, has garnered significant interest in various fields of science and technology, including sensing applications like SPR sensors. Graphene is biocompatible and exhibits low cytotoxicity, making it suitable for biomedical sensing applications. Functionalized graphene layers on SPR sensor surfaces can selectively bind to target molecules, enabling sensitive and specific detection of chemical analytes, such as gases and environmental toxins. The carrier mobility and fermi velocity of graphene are 200,000 cm^2/Vs at room temperature and 10^6m/s. respectively, making it one of the most conductive materials known [24].

Furthermore, black phosphorus (BP) is the most reliable and commonly acknowledged two dimensional (2D) material for boosting sensor capabilities due to its higher adsorption energy and capacity to bind biomolecules [25], [26]. The electrical conductivity of BP is typically on the order of ~10^3 S/m in the plane and ~10^{-4}S/m perpendicular to the layers. Additionally, its carrier mobility can exceed 1000 cm^2/Vs at room temperature, making it suitable for high-speed electronic devices [27].

Inspired by these exceptional properties of the considered layer, this article presents the performance enhancement of SPR sensor for the detection of *H. pylori* by employing two sensors. Sensor 1 has a prism-Ag-TiO_2-graphene-BP-sensing medium (SM) and sensor 2 has prism-Au-$\mathrm{TiO_2}$-graphene-BP-SM structure. The benefit of using six-layered proposed sensors is shown in the manuscript in terms of sensitivity, quality factor, dip of figure of merit and combined sensitivity factor. The sensors provide the deeper resonance dip and high resonance shift compared to other structures, which leads to the better performance as a result of high SPW length that absorbs the more transmittance light. The use of different metal oxides or

This article has been accepted for publication in IEEE Sensors Journal. This is the author's version which has not been fully edited and content may change prior to final publication. Citation information: DOI 10.1109/JSEN.2024.3409535

high RI of titanium dioxide over the metal layer can also greatly improve the sensitivity of the biosensor [23]. Moreover, the 2D materials, graphene and BP, is employed over the Titanium dioxide to increase the more absorption capacity, which leads high performance in terms of sensitivity of the SPR sensor [21]. The following is a representation of the proposed work for *H-pylori* detection: The suggested sensor's design and modelling are discussed in Section II. The description of the results simulated for the proposed study using MATLAB and COMSOL Multiphysics software is included in Section III. Finally, Section IV brings the conclusion of the proposed work.

II. DESIGN CONSIDERATION AND METHODOLOGY

This section provides the proposed sensor's design considerations and methodology along with the mathematical

A. Design Considerations

As depicted in Fig. S1 (supplementary file), in this work, we propose two sensors. The proposed sensor is designed based on the Kretschmann configuration due to the Kerr-effect. For light coupling, we optimize the prism glass by analyzing the sensitivity performance of different prisms, such as BK7, BAF10, BAK1 and SF10, which have RIs of 1.515 [24], 1.5704 [21], 1.6671 [21] and 1.7231 [21], respectively, at wavelength of 633 nm [17], [22], [26]. Furthermore, sensors 1 and 2 comprise Ag and Au, respectively, as a metallic layer, which is coated on prism's surface to generate the surface plasmons. The RI values for Ag and Au are 0.059 + 4.243i and 0.13767+3.79917i [26], [27]. The metallic layer's thickness is optimized by using the iteration method and because of that, its thickness varies with respect to the dielectric layer, which is in contact with the metallic layer [27]. TiO_2 deploys over metallic with RI of 2.5836 and thickness of T×5 nm to protect the metallic layer from its corrosion, where T stands for number of TiO_2 layers [24], [27]. Subsequently, graphene and BP are deposited over TiO_2 with RI of 3+1.1487i and 3.5+0.01i and thickness of B×0.53 and G×0.34 nm, respectively, where B and G stand for number of graphene and BP layers, respectively [24], [27], [28]. Finally, the sensing medium is placed over BP, and it contains presence of *H. pylori* sample, having RI values of 1.322, 1.324, 1.326, 1.328, 1.330, 1.332, 1.334, 1.336 and 1.338 [28].

B. Methodology

The transfer matrix technique (TMM), which is highly effective, and doesn't require any approximations, is frequently used in the multilayer modelling to determine the sensor's reflection intensity [14]-[16]. As mentioned, Eq. (1), the maximum energy of incident light will be absorbed by the sensor at resonance conditions, observing minimum reflectance (R_{min}) at the detector's side. The angle where R_{min} occurs is known as resonance angle (θ_{SPR}). Eq. (2) provides a mathematical representation of θ_{SPR} [24]. The symbols n_p, n_m and n_s is RI of the prism, metallic layer and SM, respectively, in these equations [21]. Eqs. (3) and (4) can be used to determine the reflectivity (F_p) and its coefficient (f_p) [15], [26]. The definitions of the various parameters included in Eqs. (3) and (4) are found in Eqs. (5) to (9). The transverse RI of the x^{th} layer, as provided by Eq. (5), is represented by b_N [15], [26]. expressions to measure the reflectivity (F_p) and sensing parameters.

The characteristics matrix of the integrated sensor structure (V_{if}) for p-polarized incident light is also displayed in Eq. (6).

Similarly, Eq. (7) reveals that β_x is the arbitrary stage constant for the x^{th} layer. Additionally, Eqs. (8) and (9) for θ_x and z_x, respectively, show the characteristics of the input angle and wave impedance at the x^{th} layer. In this case, μ_x, ε_x and d_x stand for the x^{th} layer's thickness, permittivity, and permeability, respectively [22].

$$\theta_{SPR} = \left(sin\sqrt{\frac{n_m^2 n_s^2}{n_p^2(n_m^2+n_s^2)}}\right)^{-1} \tag{2}$$

$$F_p = f_p f_p^* = \left|f_p\right|^2 \tag{3}$$

$$f_p = \frac{(V_{11}+V_{12}b_N)-(V_{21}+V_{8522}b_N)}{(V_{11}+V_{12}b_N)+(V_{21}+V_{22}b_{81N})} \tag{4}$$

$$b_x = \begin{bmatrix}\mu_x \\ \varepsilon_x\end{bmatrix}^{1/2} \qquad cos\,\theta_x = \sqrt{\frac{\varepsilon_x-(n_p\,sin\,\theta)^2}{\varepsilon_x^2}} \tag{5}$$

$$V_{if} = \left[\prod_{x=2}^{N-1}\begin{pmatrix}cos\,\beta_x & -i\,sin\,\beta_x \\ -in_x sin\,\beta_x & cos\,\beta_x\end{pmatrix}\right]_{if} = \begin{bmatrix}Z_{11} & Z_{12} \\ Z_{21} & Z_{22}\end{bmatrix} \tag{6}$$

$$\beta_x = \frac{2\pi}{\lambda} r_x\,cos\,\theta_x\,(s_x - s_{x-1}) = \frac{2\pi}{\lambda} d_x\sqrt{\varepsilon_x - (r_p\,sin\,\theta)^2} \tag{7}$$

$$\theta_x = \left(cos\sqrt{1-(b_{x-1}/b_x)(sin\,\theta)^2}\right)^{-1} \tag{8}$$

$$s_k = \frac{w_x b_k\,cos\,\theta_k}{(2\pi c/\lambda_{633})\varepsilon_k^2} \tag{9}$$

Moreover, Eq. (10) shows the reflectivity formula for the proposed sensor's six-layered structure once the aforementioned mathematical relations are incorporated [28]. Here, f_{12}, f_{23}, f_{34}, f_{45}, f_{56} and f_{67} represent the reflected intensities between respected layers, whereas d_m and w_x respected layer's thickness and wave vector component [15].

$$F_{123456} = |f_{123456}|^2 = \left|\frac{f_{12}+f_{23456}\ e^{2iw_2d_2}}{1+f_{12}\ f_{23456}\ e^{2iw_2d_2}}\right|^2 \tag{10}$$

$$f_{23456} = \frac{f_{23}+f_{3456}\ e^{2iw_3d_3}}{1+f_{23}\ f_{34567}\ e^{2iw_3d_3}},\quad f_{3456} = \frac{f_{34}+f_{456}\ e^{2iw_4d_4}}{1+f_{34}f_{4567}e^{2iw_4d_4}},\quad f_{456} = \frac{f_{45}+f_{567}\ e^{2iw_5d_5}}{1+f_{45}f_{56}e^{2iw_5d_5}},\quad f_{12} = \frac{\varepsilon_2/w_2-\varepsilon_1/w_1}{\varepsilon_2/w_2+\varepsilon_1/w_1}, f_{23} = \frac{\varepsilon_3/w_3-\varepsilon_2/w_2}{\varepsilon_3/w_3+\varepsilon_2/w_2},\quad f_{34} = \frac{\varepsilon_4/w_4-\varepsilon_3/w_3}{\varepsilon_4/w_4+\varepsilon_3/w_3}, f_{45} = \frac{\varepsilon_5/w_5-\varepsilon_4/w_4}{\varepsilon_5/w_5+\varepsilon_4/w_4}, f_{56} = \frac{\varepsilon_6/w_6-\varepsilon_5/w_5}{\varepsilon_6/w_6+\varepsilon_5/w_5}$$

In this work, we analyze the sensor performance in terms of sensitivity, QF, DFoM and CSF. The mathematical form of these sensing parameters is represented in Eq. (11-14). Where, $\nabla\theta_{res}$, ∇n, FWHM, R_{max} and R_{min} stand for deviation in SPR resonance angle, deviation in RI of analytes, Full-width half-maxima, maximum and minimum reflectance of SPR curve, respectively. FWHM refers to the SPR spectrum's amplitude at 50% reflectivity. The sensor's sensing capability, quality, resolution, and overall performance are displayed by the metrics, respectively. In order to optimize SPR-based sensors for biological and biomedical applications, it is necessary to achieve the highest feasible performance parameters [15], [21], [23], [24].

This article has been accepted for publication in IEEE Sensors Journal. This is the author's version which has not been fully edited and content may change prior to final publication. Citation information: DOI 10.1109/JSEN.2024.3409535

$$Sensitivity = \nabla\theta_{res}/\nabla n \qquad (°/RIU) \qquad (11)$$

$$QF = Sensitivity/FWHM \qquad (RIU^{-1}) \qquad (12)$$

$$DFoM = Sensitivity/R_{min} \qquad (13)$$

$$CSF = Sensitivity \times [(R_{max} - R_{min})/FWHM] \qquad (14)$$

III. RESULTS AND DISCUSSION

Initially, we have optimized the metal layers' thicknesses and prism for Sensors 1 and 2 by observing the performance of minimum reflectance and sensitivity by applying the iteration process of Fresnel's mode analysis with the transfer matrix method (TMM). Then, in order to show optimized structure, we have considered another seven structures with defined layers and analyzed the SPR performance parameters for each structure. This study mainly focuses on the SPR sensitivity performance because in the literature study, it has been found that sensitivity is one of the most important parameters for analyzing a high-performance SPR biosensor. Moreover, many researchers have been explored several structures in order to improve the SPR sensitivity performance only [15]. Additionally, this study measures the performance of QF, DFoM and CSF [21]. Subsections also address the assessment of sensor performance parameters for different RI of *H. pylori* samples, a comparison with the previously published research and lastly, the distribution of field at the proposed SPR sensor's layer interface using COMSOL Multiphysics software.

A. Optimal Metal Layer Thickness

Optimization of metal thickness plays an important role while analyzing the sensor performance as it affects reflectivity. Reflectivity quantifies the level of incident light reflected from the sensor surface and exhibits an inverse relationship with sensitivity. Decreased reflectivity improves sensitivity, thereby aiding in the detection of minute variations in RI [26]. As the first observation, this study analyzes the optimal Ag thickness for the proposed sensor. Fig. 1(a) illustrates the change in reflectance across a broad range of angles of incidence for different thicknesses of Ag layer for sensor 1, configured as BK7-Ag-TiO$_2$-graphene-BP-SM. The RI of the SM is kept at 1.322. Further, Fig. 1(a) demonstrates a significant improvement in R$_{min}$ with Ag layer thickness increasing from 40 to 51 nm. Fig. 1(b) illustrates the minimum reflectance (R$_{min}$) curve varies with Ag layer thickness. It is observed from figure that the R$_{min}$ achieved at 51 nm of Ag thickness. Similarly, Fig. 1(c) depicts variations in reflectance concerning incidence angle for various thicknesses of the Au layer for sensor 2, structured as BK7-Au-TiO$_2$-graphene-BP-SM. Moreover, the R$_{min}$ achieved at 45 nm of Au thickness, as depicted in Fig. 1(d).

B. Optimal Prism

Choosing the prism material is a vital factor in designing SPR-based sensor, impacting sensitivity, angular range, and overall performance. The prism's function is to channelize light onto the sensor surface, enabling the activation of SPs and the detection of variations in the RI of the surrounding medium. In Fig. 2(a), reflectance curves are displayed across incident angles for various prism glasses corresponding to the SM with

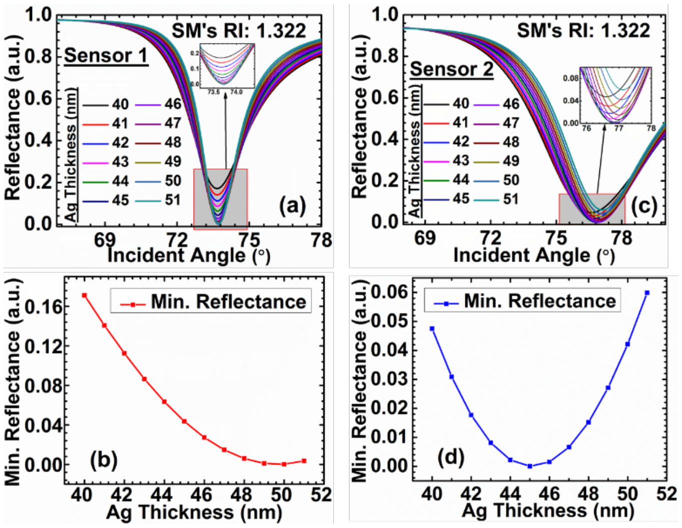

Fig. 1. (a) Reflectance vs an incident angle for different Ag thickness using sensor 1, (b) R_{min} vs Ag thickness for sensor 1. (c) Reflectance vs an incident angle for different Ag thickness using sensor 2, and (d) R_{min} vs Ag thickness for Sensor 2.

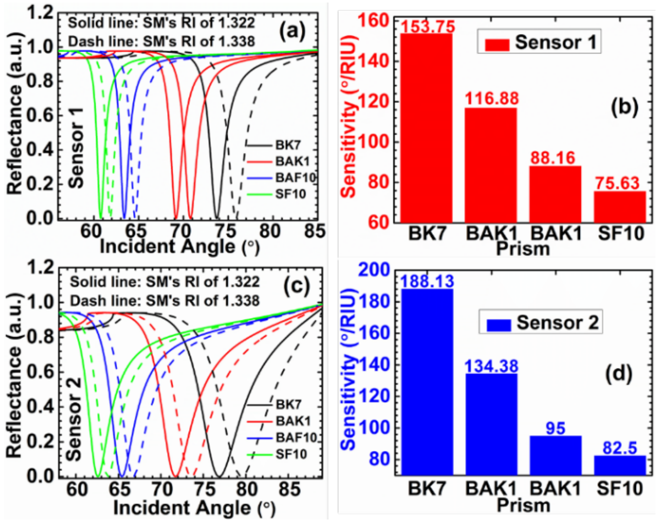

Fig. 2. (a) Reflectance vs an incident angle for different prisms using sensor 1, (b) R_{min} vs Prism for sensor 1. (c) Reflectance vs an incident angle for different prisms using Sensor 2, and (d) R_{min} vs Prism for Sensor 2.

RIs of 1.322 and 1.338 for sensor design 1. Fig. 2(b) displays the sensitivity response for sensor 1 with various prisms, including BK 7, BAK 1, BAF 10, and SF 10. It is noted that the maximum angular sensitivity of 153.75 °/RIU is achieved with the BK7 prism. Likewise, Fig.2(c) demonstrates the variation in R$_{min}$ with different prisms considered for sensor design 2. The highest sensitivity of 188.13 °/RIU is observed with BK7, as shown in Fig. 2(d).

C. Optimization of Structure

Fig. 3(a) demonstrates the reflection intensity relative to the angle of incidence for sensor design 1, highlighting several possible combinations. Among these, BK7-Ag-TiO$_2$-graphene-BP is considered as the potential combination as it provides the largest angular shift between the SMs of RI 1.322 and 1.338. Notably, the solid line indicates the variation in reflection intensity aligned with incident light characterized by SM's RI

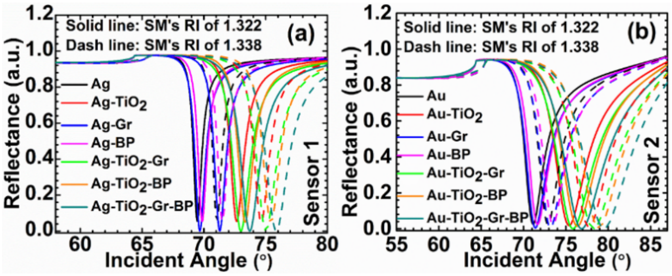

Fig. 3. (a) Reflectance vs an incident angle for different considered structures for sensor 1 and (b) Reflectance vs an incident angle for different considered structures for sensor 2.

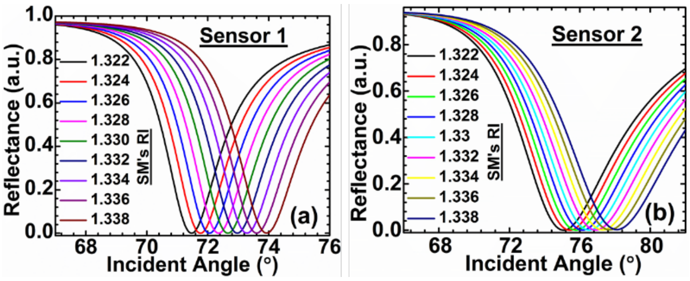

Fig. 4(a) Reflectance vs an incident angle for different RI values of SM using sensor 1 and (b) Reflectance vs an incident angle for different RI values of SM using sensor 2.

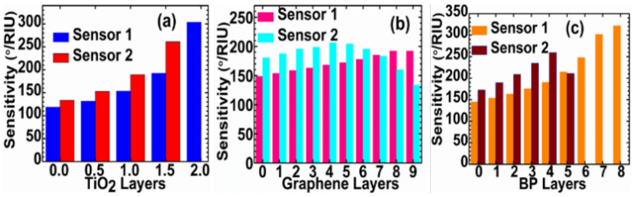

Fig.5 Measured Sensitivity (a) Vs TiO_2 layers (b) Vs Graphene layers. (b) Vs BP layers.

of 1.3348, while the dashed line portrays the reflection intensity corresponding to a SM of RI 1.3398. The maximum angular sensitivity achieved with sensor 1 is 321.43 °/RIU. The shift towards higher angles in the resonance angle is evident for the configurations of Ag-TiO_2-BP, Ag-TiO_2-Gr-BP, Au-TiO_2-BP, and Au-TiO_2-Gr-BP, as depicted in Figs. 3(a) and (b). This shift is attributed to the substantial RI of the 2D materials. In Fig. 3(a), the changes in resonance angle are found to be 1.8°, 2.28°, 1.84°, 1.87°, 2.31°, 2.42°, and 2.45° for the corresponding structure (BK7-Ag-TiO_2-graphene-BP) listed in Table S1 (supplementary file). Similarly, in Fig. 3(b), the changes in resonance angle are 2.01°, 2.69°, 2.04°, 2.08°, 2.76°, 2.89° and 3.03° for the respective structure (BK7-Au-TiO_2-graphene-BP) provided in Table S2 (supplementary file). Notably, sensor 2 exhibits a wider reflectance curve compared to sensor 1, attributed to the high RI of the Au layer.

D. Detection Process

After optimizing the prism and metallic layer thickness for sensors 1 and 2, this section shows the performance analysis of proposed sensors for the detection of *H. pylori*. For this event, the RI of SM is varied from 1.322 to 1.338 with an interval of 0.002, which are considered in the literature. The optimized structures are Ag (50 nm)/TiO_2 (5 nm)/Graphene (0.34 nm)/BP (0.53 nm) for sensor 1 and Au (45 nm)/ TiO_2 (5 nm)/Graphene (0.34 nm)/BP (0.53 nm) for sensor 2. Fig. 4(a) depicts the reflectance curves with respect to incident angle for different considered SM's RI values for sensor 1, whereas Fig. 4(b) for sensor 2. The observed discrepancies in the curves can be attributed to variations in SM's RI, which in turn affects variations in SPW length and penetration depth (PD), resulting in higher FWHM. The obtained parameters of resonance angle (θ_{res}), FWHM, R_{min} and maximum reflectance (R_{max}) values for each curve of Figs. 4(a) and 4(b) are reported in Table S3 (supplementary file) and S5 (supplementary file), where Table S3 for sensor 1 and TABLE S5 for sensor 2. It can be easily identified that sensor 2, which comprised Au as metallic layer, provides higher FWHM values when compared to the sensor 1, which has Ag as metallic layer. The FWHM observed in Au compared to Ag is large due to Au's greater electron scattering and significant interband transitions that occur within the visible spectrum, both of which lead to greater damping of plasmonic resonances. This makes Au nanoparticles exhibit broader resonance peaks, which can lead poor sensor resolution. The sensing parameters for Figs. 4(a) and 4(b) are measured by applying Eqs. (12) to (15) and noted in Table S4 (supplementary file) and S6, where Table S4 for sensor 1 and Table S6 for sensor 2. It is clearly observed that the sensitivity performance is less with sensor 2 when compared with the sensor 1. The higher sensitivity associated with Au is due to its superior chemical stability, biocompatibility, and the advantageous optical properties of its plasmon resonance. These factors make Au particularly suited for sensitive detection mechanisms in biosensing, environmental sensing, and other analytical applications.

Due to its higher SPR ratio and sharp resonance dip, Ag-based sensor 1 affords better QF, DFoM and CSF performance while compared to sensor 2. Therefore, from this study, it is concluded that sensor 1 can be used as a better quality and resolution device, whereas sensor 2 utilizes for better sensing device. Notably, the performance is obtained at change in RI of 0.014 for sensor 1 and 0.016 for sensor 2, which will be used for further analysis of the study.

Moreover, Fig. 5(a) depicts the graphical representation of measured sensitivity with respect to the TiO_2 layers, whereas the thicknesses of residual layers are kept constant. Number of TiO_2 layers are varied from 0 to 2 and 0 to 1.5 for sensor 1 and 2, respectively, with an interval of 0.5. The SPR property is not fulfilled at number of TiO_2 layers are greater than 2 and 1.5 for sensors 1 and 2, respectively. The measured sensitivities are 118.57, 131.43, 153.57, 192.14 and $303.57°/RIU$ at TiO_2 layer of 0, 0.5, 1, 1.5 and 2, respectively, using sensor 1. Similarly, 133.75, 153.125, 189.375 and $261.25°/RIU$ at TiO_2 layer of 0, 0.5, 1 and 1.5, respectively, using sensor 2. The amount of sensitivity varies because of changes in the layers' thickness that cause changes in the PD and length of the SPW [25].

Furthermore, Fig. 5(b) shows the graphical representation of measured sensitivity with respect to the graphene layers, whereas the thicknesses of residual layers are kept constant. Number of graphene layers are varied from 0 to 9 for both sensors 1 and 2, with an interval of 1. The SPR property is not

This article has been accepted for publication in IEEE Sensors Journal. This is the author's version which has not been fully edited and content may change prior to final publication. Citation information: DOI 10.1109/JSEN.2024.3409535

fulfilled at number of graphene layers are greater than 9 for both sensors 1 and 2. The attained sensitivities are from 148.57 to $192.14^\circ/RIU$ for sensor 1, 133.75 to $206.25^\circ/RIU$ for sensor 2. The sensitivity is increased with the number of TiO_2 layers when compared with the number of graphene layer due to its high RI and dielectric constant, can enhance the sensitivity of optical sensors through stronger light-matter interactions than graphene. Likewise, Fig. 5(c) illustrates the graphical representation of measured sensitivity with respect to BP layer, whereas the thicknesses of residual layers are kept constant. Number of BP layers are varied from 0 to 9 and 0 to 5 for both sensors 1 and 2, respectively with an interval of 1. The SPR property is not fulfilled at number of graphene layers are greater than 8 and 5 for sensors 1 and 2, respectively. The attained sensitivities range from 144.86 to $321.43^\circ/RIU$ for sensor 1 and 172.50 to $259.375^\circ/RIU$ for sensor 2. Sensitivity is increased with the number of TiO_2 layers when compared with the number of graphene layer due to its high RI and dielectric constant, can enhance the sensitivity of optical sensors through stronger light-matter interactions than graphene. It can be observed that the sensitivity is increased with number of BP layers while comparing with number of TiO_2 and graphene layers. The increased sensitivity of BP compared to TiO_2 and graphene can be attributed to its tunable bandgap, balanced carrier mobility, anisotropic properties, and surface reactivity. These features make BP an attractive material for a range of applications, including sensors, photodetectors, and other optoelectronic devices, where its ability to absorb a wide spectrum of light and its tunable electrical properties can be leveraged to achieve high sensitivity and specificity [26-28]. From this study, it is concluded that the maximum sensitivity performance is achieved using structures of BK7/Ag (50 nm)/TiO_2 (5 nm)/graphene (0.34 nm)/BP (8×0.53 nm)/SM for sensor 1, and BK7/Au (45 nm)/TiO_2 (1.5 ×5 nm)/graphene (0.34 nm)/BP (0.53 nm)/SM for sensor 2. Finally, we also computed QF, DFoM, and CSF for these sensors. It is found that the obtained QF, DFoM and CSF are $57.09 RIU^{-1}$, 5974.53 and 52.63 for sensor 1, and $30.41 RIU^{-1}$, 22,139.83 and 28.21 for sensor 2.

E. Comparative study on Performance analysis

In this section, the performance of proposed SPR sensors is compared with the existing sensor for the detection of *H. pylori*, as shown in Table VII. Dyankov *et al.*, [29] presented a long period grating (LPG)-based biosensor for the *H. pylori* detection and achieved the maximum sensitivity of 3000 CFU/mL. Moreover, Singh *et al.*, [27] also suggested an SPR-based biosensor for *H. pylori* detection employing Au and silicon oxynitride, and they obtained the sensing parameters, which are reported in Table I. It can be witnessed that the proposed sensors provide the better performance compared to existing sensors. Additionally, the proposed sensor computes the CSF, which can manifest the overall performance of the sensor.

TABLE I
COMPARATIVE STUDY ON PERFORMANCE ANALYSIS

Reference	[27]	[29]	Proposed work 1	Proposed work 2
Sensor type	SPR	LPG	SPR	
Sensitivity ($^\circ/RIU$)	185	3000 CFU/Ml	321.43	261.25
QF (RIU^{-1})	25.77	-	57.09	30.41
DFoM	0.41	-	5974.53	22,139.83
CSF	-	-	52.63	28.21

F. Field Distributions of Proposed Sensors Using COMSOL Software

Two additional critical parameters, penetration depth (PD) and normalized electric field distribution, which differ from conventional parameters, are crucial for a thorough analysis of the proposed SPR sensor's performance. The analysis of surface plasmon field pattern and PD in the sensing medium is done by means of the finite element method (FEM). The mathematical model of the proposed SPR sensor configuration is simulated using the FEM method and the COMSOL Multiphysics software. The electric field intensity for the proposed sensor incorporating BK7/Ag (50 nm)/TiO_2 (5 nm)/graphene (0.34 nm)/BP (0.53 nm)/SM is dependent on the distance from the prism to the sensing medium, as illustrated in Fig. 6(a). The simulation was carried out utilizing a sensing medium with a wavelength of 633 nm and RI of 1.322 and 1.338. Remarkably, the electric field intensity at the BP-sensing medium interface is dependent on the thickness of all the layers for a given sensor and reaches its maximum at a specific thickness. The highest field intensity is attained at SM's RI of 1.322 (7.7×10^4 V/m) and SM's RI of 1.338 (5.5×10^4 V/m). The PD values measured for both sensing media (1.3348 and 1.3398) are 144.96 nm and 142.28 nm. Approximately, 37% of the PD is dependent on the 1/e factor. The maximum field intensity can be clearly seen at the interface between the BP and the sensing medium. The electric field is exponentially decreasing in the sensing medium. The collective oscillation of electrons at the interface of a metal layer and a dielectric medium is described by surface plasmon polaritons (SPPs). SPPs are evanescent waves that travel along the metal-dielectric interface. When the incident light's angle is equal to the angle required to excite SPPs, resonance occurs. The coupling between the incident light and the SPPs causes the reflectance curve to dip. The SPP mode is greatly affected by variations in the dielectric media's RI in the vicinity of the BP surface. This sensitivity is used by SPR sensors to monitor binding events in real time, such as biomolecular interactions on the sensor surface. Fig. 6(b) displays the SPPs mode in both 2D and 3D. The maximum sensitivity to the RI of 1.322 for the BP-sensing medium can be determined by employing the SPP modes. Figs. 6(b) and 6(c) display 2D and 3D field distribution plots. Figs. 6(d) and 6(e) show the variations of the y-component of the electric field distribution along the layers interface of the proposed sensor.

Moreover, Fig. 7(a) illustrates the proposed SPR sensor layer wise 1D field plot. When looking toward the z-axis, the peak value of the normalized electric field divided by 1/e, or 37%, is the PD of the TM field from the interface as shown in Fig. 7(b). It is evident that the electric field is stronger at the interface and decays exponentially in the direction of the sensing media. The maximum field intensities 1.64×10^5 V/m and 1.61×10^5 V/m are achieved for SM's RI of 1.322 and 1.338, respectively. At both sensing mediums, the normalized electric fields are overlapping due to marginal gap between RI of SM. Attained PD of 145.12 nm for SM's RI of 1.322 and 144.41nm for SM's RI of 1.338. At the interface between the BP and the sensing medium, the induced electromagnetic field spikes (2D plot) of SPPs are depicted in Fig. 8(b). Also, the 3D plot of SPP mode is shown in Fig. 7(c). Further, the electric field distribution for the proposed SPR sensor in the form of 2D plot and 3D plot is shown in Figs. 7(d) and 7(e).

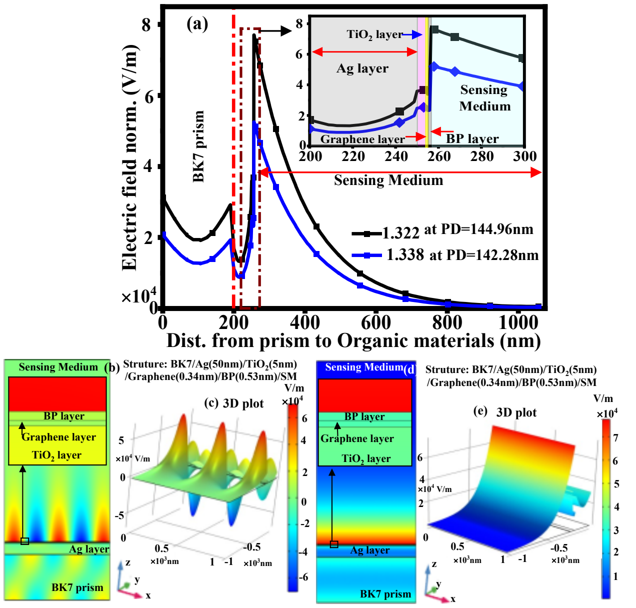

Fig. 6 (a) Normalized electric field (b) 2D SPP mode (c) 3D SPP mode (d) 2D electric field distribution (e) 3D electric field distribution.

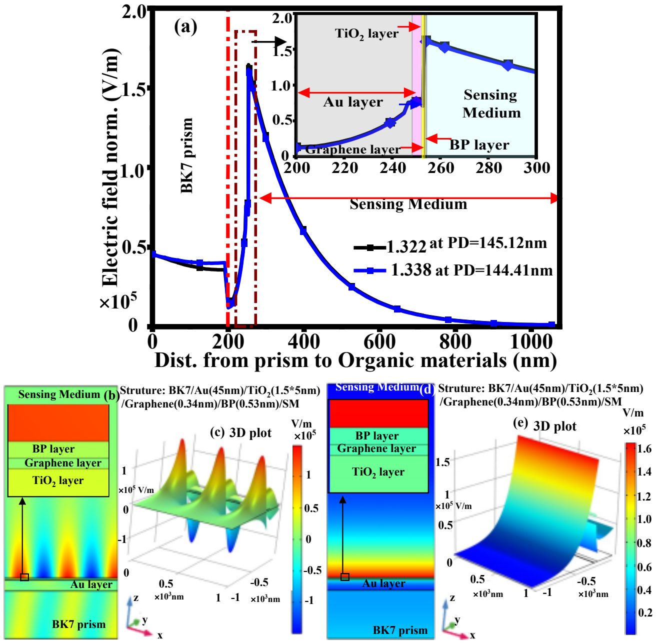

Fig. 7 (a) Normalized electric field (b) 2D SPP mode (c) 3D SPP mode (d) 2D electric field distribution (e) 3D electric field distribution for Sensor 2.

G. *Required Fabrication Steps for Development*

The schematic experimental setup feasibility for the proposed sensor is illustrated in Fig. 8. The substrate of the sensor is a BK7 prism. First, methanol, acetone, and deionized water are used to clean the prism's surface [29]. Using e-beam deposition equipment, a TiO_2 layer can first be placed onto the prism or glass substrate [29]. The physical vapour deposition (PVD) method can then be used to deposit more layers of materials, such as Au and Ag [25]. Moreover, a number of methods, such as chemical vapour deposition (CVD) or plasma-enhanced CVD can be used to deposit the TiO_2 layer [30]. The resulting TiO_2 layer can be evaluated for quality, thickness, and structural characteristics using methods like X-ray photoelectron spectroscopy (XPS), Raman spectroscopy, atomic force microscopy (AFM), and scanning electron microscopy (SEM). This configuration is intended for sensing applications. Atomic layer deposition (ALD) or pulsed laser deposition (PLD) can be used to deposit the graphene atop TiO_2 film [30], [31]. Subsequently, the CVD process can be used to deposit BP [15]. It is now possible to apply the biosample to the TiO_2 layer to carry out the sensing operation. As of right now, the arrangement calls for rotating the sensor structure and determining the resonance angle with a goniometer. A photodetector is used to measure and record the reflected light on the other face of the prism when a monochromatic p-polarized light beam is directed towards one of its faces. Culturing Helicobacter pylori, a bacterium requires specific conditions due to its unique growth requirements. This bacterium thrives in the acidic environment of the stomach by producing urease, an enzyme that converts urea to ammonia, which helps neutralize the acid in its immediate vicinity. When attempting to culture *H. pylori* in a laboratory setting, these physiological needs must be replicated as closely as possible.

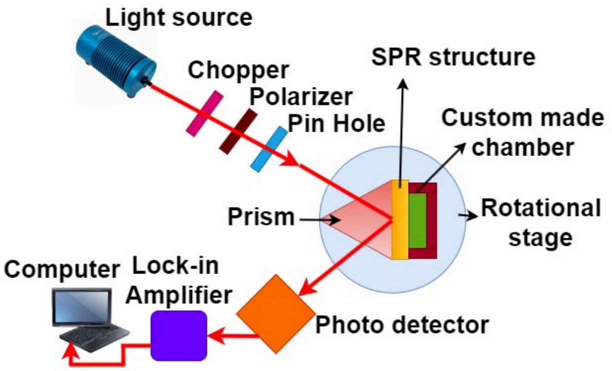

Fig. 8. Schematic experimental setup feasibility of proposed SPR sensor.

IV. CONCLUSION

Two SPR sensors are proposed in this paper for the detection of *H. pylori* at wavelength of 633 nm using the angular interrogation technique. The optimization of prism and metallic layer thickness is shown by observing the better sensitivity and R_{min} performances, resulting BK7 glass, Ag thickness of 50 nm and Au thickness of 45 nm. Subsequently, structure optimization is shown by measuring sensitivity performance for different structures, which are made-up with defined layers of sensors 1 and 2 and observed that sensors 1 and 2 provide better sensitivity compared to others.

Furthermore, the detection of *H. pylori* is executed with help of optimized sensors 1 and 2 for nine different samples of *H. pylori*. Additionally, sensitivity performance is measured for different layers of TiO_2, graphene and BP. The maximum accomplished performances are sensitivity of $321.43°/RIU$, a QF of $57.09\ RIU^{-1}$, a DFoM of 5974.53 and a CSF of 52.63 for sensor 1, and sensitivity of $261.25°/RIU$, a QF of $30.41 RIU^{-1}$, a DFoM of 22,139 and a CSF of 28.21 for sensor 2, which demonstrate extreme enhancement in comparison to the reported work in literature. Additionally, the manuscript provides the possible fabrication steps that are involved in the development of SPR chip, which shows the feasibility of the present work to readers.

REFERENCES

[1] A. Oliva, A. Spira, and L. Multigner, “Contribution of environmental factors to the risk of male infertility,” *Hum. Reprod.*, vol. 16, no. 8, pp. 1768–1776, 2001.

[2] V. M. Brugh, H. M. Matschke, and L. I. Lipshultz, “Male factor infertility,” *Endocrinol. Metab. Clin.*, vol. 32, no. 3, pp. 689–707, 2003.

[3] J. Evans *et al.*, “Fresh versus frozen embryo transfer: backing clinical decisions with scientific and clinical evidence,” *Hum. Reprod. Update*, vol. 20, no. 6, pp. 808–821, 2014.

[4] J. Wang and M. V Sauer, “In vitro fertilization (IVF): a review of 3 decades of clinical innovation and technological advancement,” *Ther. Clin. Risk Manag.*, vol. 2, no. 4, pp. 355–364, 2006.

[5] G. Stamenov, D. Parvanov, T. Chaushev, D. Baltadzhieva, I. Iliev, and B. Dzhambazov, “Approaches for prediction of the implantation potential of human embryos.,” *J. Biosci. Biotechnol.*, vol. 2, no. 2, 2013.

[6] D. Mortimer and S. T. Mortimer, “Computer-aided sperm analysis (CASA) of sperm motility and hyperactivation,” *Spermatogenes. Methods Protoc.*, pp. 77–87, 2013.

[7] M. Tomlinson, J. Turner, G. Powell, and D. Sakkas, “One-step disposable chambers for sperm concentration and motility assessment: how do they compare with the World Health Organization’s recommended methods?,” *Hum. Reprod.*, vol. 16, no. 1, pp. 121–124, 2001.

[8] M. I. Newton *et al.*, “Low-cost QCM sensor system for screening semen samples,” *J. Sensors*, vol. 2010, 2010.

[9] S. Atherton, *Semen quality detection using acoustic wave sensors*. Nottingham Trent University (United Kingdom), 2011.

[10] M. V. P. Chowdary, K. K. Kumar, J. Kurien, S. Mathew, and C. M. Krishna, “Discrimination of normal, benign, and malignant breast tissues by Raman spectroscopy,” *Biopolym. Orig. Res. Biomol.*, vol. 83, no. 5, pp. 556–569, 2006.

[11] F. Liu *et al.*, “Real-time Raman microspectroscopy scanning of the single live sperm bound to human zona pellucida,” *Fertil. Steril.*, vol. 99, no. 3, pp. 684–689, 2013.

[12] K. Ahmed *et al.*, “Refractive index-based blood components sensing in terahertz spectrum,” *IEEE Sens. J.*, vol. 19, no. 9, pp. 3368–3375, 2019.

[13] K. Ahmed *et al.*, “Design of D-shaped elliptical core photonic crystal fiber for blood plasma cell sensing application,” *Results Phys.*, vol. 12, pp. 2021–2025, 2019.

[14] M. A. Jabin, K. Ahmed, M. J. Rana, B. K. Paul, Y. Luo, and D. Vigneswaran, “Titanium-coated dual-core D-shaped SPR-based PCF for hemoglobin sensing,” *Plasmonics*, vol. 14, no. 6, pp. 1601–1610, 2019.

[15] L. Singh, Y. Vasimalla, V. Dhasarathan, J. S. Skibina, A. Y. Gryaznov, and S. S. Konnova, “A highly sensitive refractive index based etched optical fiber sensor for detection of human sperm,” *Opt. Lasers Eng.*, vol. 169, p. 107727, 2023.

[16] E. Klantsataya, A. François, H. Ebendorff-Heidepriem, P. Hoffmann, and T. M. Monro, “Surface plasmon scattering in exposed core optical fiber for enhanced resolution refractive index sensing,” *Sensors*, vol. 15, no. 10, pp. 25090–25102, 2015.

[17] V. Yesudasu, H. S. Pradhan, and R. J. Pandya, “Recent progress in surface plasmon resonance based sensors: A comprehensive review,” *Heliyon*, vol. 7, no. 3, 2021.

[18] V. Yesudasu and H. S. Pradhan, “Performance enhancement of a novel surface plasmon resonance biosensor using thallium bromide,” *IEEE Trans. Nanobioscience*, vol. 21, no. 2, pp. 206–215, 2021.

[19] G. Li, R. Singh, J. Guo, B. Zhang, and S. Kumar, "Nb_2CTx MXene-assisted double S-tapered fiber-based LSPR sensor with improved features for tyramine detection," Applied Physics Letters, Vol. 122, p. 083701, Feb. 2023.

[20] R. Jha, P. Mishra, and S. Kumar, "Advancements in optical fiber-based wearable sensors for smart health monitoring," Biosensors and Bioelectronics, Vol. 254, p. 116232, June 2024.

[21] Y. Vasimalla, H. Shekhar Pradhan, and R. Jashvantbhai Pandya, “SPR performance enhancement for DNA hybridization employing black phosphorus, silver, and silicon,” *Appl. Opt.*, vol. 59, no. 24, p. 7299, 2020, doi: 10.1364/ao.397452.

[22] Z. Yin, X. Jing, K. Li, Z. Zhang, and J. Li, “Modulation of the sensing bandwidth of dual-channel SPR sensors by TiO_2 film,” *Opt. Laser Technol.*, vol. 169, p. 110105, 2024.

[23] J. Divya, S. Selvendran, A. S. Raja, and K. Chitra, “Silver-Tio_2 coated d-shaped photonic crystal fiber based spr sensor for ultrasensitive refractive index detection: design and fem analysis,” *Phys. Scr.*, vol. 99, no. 2, p. 25505, 2024.

[24] Y. Vasimalla and L. Singh, “Design and analysis of planar waveguide-based spr sensor for formalin detection using Ag-Chloride-BP structure,” *IEEE Trans. Nanobioscience*, vol. 22, no. 2, pp. 365–374, 2022.

[25] K. M. Ishtiak, S.-A. Imam, and Q. D. M. Khosru, “BaTiO3-Blue Phosphorus/WS_2 hybrid structure-based surface plasmon resonance biosensor with enhanced sensor performance for rapid bacterial detection,” *Results Eng.*, vol. 16, p. 100698, 2022.

[26] P. Li, B. Liu, B. Shen, J. Zhai, L. Li, and H. Zeng, “Large strain response in Bi4Ti3O12 modified BNT-BT piezoelectric ceramics,” *Ceram. Int.*, vol. 43, no. 1, pp. 1008–1013, 2017.

[27] L. Singh, Y. Vasimalla, R. Kumar, and P. Pareek, “Highly sensitive surface plasmon resonance sensor for refractive index detection of Helicobacter Pylori,” *Optik (Stuttg).*, vol. 274, p. 170516, 2023.

[28] J. B. Smith, D. Hagaman, and H.-F. Ji, “Growth of 2D black phosphorus film from chemical vapor deposition,” *Nanotechnology*, vol. 27, no. 21, p. 215602, 2016.

[29] G. Dyankov *et al.*, “SPR and Double Resonance LPG Biosensors for Helicobacter pylori BabA Antigen Detection,” *Sensors*, vol. 24, no. 7, p. 2118, 2024.

[30] N. R. Ramanujam, S. K. Patel, N. M. Reddy, S. A. Taya, D. Vigneswaran, and M. S. M. Rajan, “One-dimensional ring mirror-defect photonic crystal for detection of mycobacterium tuberculosis bacteria,” *Optik (Stuttg).*, vol. 219, p. 165097, 2020.

[31] N. Mao *et al.*, “Optical anisotropy of black phosphorus in the visible regime,” *J. Am. Chem. Soc.*, vol. 138, no. 1, pp. 300–305, 2016.